



# Influence of surface layers on resistance spot joinability of partially hardened steel 22MnB5 with aluminum-silicon and zinc coatings

Oleksii Sherepenko<sup>1</sup> · Vincent Schreiber<sup>1</sup> · Iwan Schischin<sup>1</sup> · Maximilian Wohner<sup>1</sup> · Philipp Wernlein<sup>1</sup> · Niels Mitzschke<sup>1</sup> · Sven Jüttner<sup>1</sup>

Received: 30 May 2019 / Accepted: 2 February 2020 / Published online: 11 March 2020  
© International Institute of Welding 2020

## Abstract

One of the methods to achieve local change in material properties when producing high strength parts with tailored mechanical properties is varying temperature histories in the furnace prior to hot stamping. This causes changes in surface layer development of coated steels and thus differences in contact resistances, which determine heat development during the resistance welding process. To get a deeper understanding of the influences, surface layers have on the welding process, parts with temperature histories, typical for industrially manufactured partially hot-stamped parts with aluminum-silicon and zinc coatings were investigated. Static contact resistance was determined; measurements of dynamic resistances in welding process were conducted. Welding current ranges were determined for different heat-treated conditions. No correlation between static contact resistance and welding current range was found; however for Zn coating, the welding current range was moved towards lower welding currents and shrunk for the measured total static contact resistance of about 4000  $\mu\Omega$ . For aluminum-silicon coating, no dependence between welding current range and static contact resistance was evident. For Al-Si-coated steel, a novel criterion, based on the fraction of the resistive phases in the surface layer, determined by metallographic investigations was developed, allowing to determine material joinability.

**Keywords** Spot welding · Metallography · Microstructure · Martensite · Hot stamping

## 1 Introduction

The fundamental investigations of the Al-Fe-Si system, covering a wide range of temperatures and compositions, are being conducted since the late 1920s and are extensively described in [1]. Since the development of press-hardening Al-Si-coated steels [2], many investigations of the phase formation in the Al and Fe-rich part of the ternary system have been conducted for

temperature, time, and composition range of Al-Si coating on the low alloyed steel in the furnace process during hot stamping [3–5]. Grigorieva et al. [3] investigate layer formation during the heating process with furnace times from 1 to 10 min and furnace temperature of 900 °C; Jenner et al. [4] use furnace temperature of 925 °C and multi-step furnace time variation to achieve different layer conditions; Windmann et al. [5] extend the time range to 30 min at furnace temperature of 920 °C, also testing

Recommended for publication by Commission III - Resistance Welding, Solid State Welding, and Allied Joining Process

✉ Oleksii Sherepenko  
oleksii.sherepenko@ovgu.de

Vincent Schreiber  
vincent.schreiber@ovgu.de

Iwan Schischin  
iwan.schischin@ovgu.de

Maximilian Wohner  
maximilian.wohner@ovgu.de

Philipp Wernlein  
philipp.wernlein@st.ovgu.de

Niels Mitzschke  
niels.mitzschke@ovgu.de

Sven Jüttner  
sven.juettner@ovgu.de

<sup>1</sup> Institute of Materials and Joining Technology (IWF), Otto-von-Guericke-University Magdeburg, Universitätsplatz 2, 39106 Magdeburg, Germany

temperatures of 950 and 1000 °C. Extensive studies of surface layer development in the furnace process for Zn-coated hot stamping steels were conducted by [6]. Determination of welding current ranges of resistance spot welded Al-Si and Zn-coated steels in similar temperature ranges can be found in [7–11].

A further development of a conventional hot stamping process—partial hot stamping allows producing high strength parts with tailored mechanical properties: locally adjusted higher fracture elongation and lower strength [1, 12]. One of industrially used methods to achieve tailored properties is variation of temperature histories in different zones of one part during the hot stamping process, so that a zone, heated above the  $Ac_3$  temperature, is transformed into the martensite during the hot stamping process, leaving the zone heated below  $Ac_1$  in soft and ductile ferritic-pearlitic condition, and a transition zone between them [13]. Altering the temperature history leads to changes in surface layer development and may therefore lead to changes in welding current ranges (WCR). For critical three-sheet stack-ups, consisting of two thick resistive hot-stamped sheets in combination with a thin outer sheet, where achieving sufficient nugget penetration depth into the thin outer sheet is an issue, changes in layer morphology when producing tailored-property parts (tpp) by partial austenitization and resulting change in heat input during the welding process have tremendous effect on welding current range, as reported by [14]. Figure 1 shows that with the use of same welding parameters and sheet stack-ups, for hot-stamped parts, heat treated with lower furnace temperatures and shorter furnace times, no nugget penetration into the thin sheet was observed, because of low heat generation at the interface between the sheets. With higher temperatures and longer furnace times, heat generation and as a result nugget penetration into the thin sheet were promoted.

Although extensive studies of surface layers for both Al-Si and Zn-coated steel 22MnB5, typically used for hot stamping

applications, are present in the literature, the amount of integral studies, incorporating investigations of layer development and its influence on welding current ranges, is limited.

For Zn-coated steels, heat treated at hot stamping relevant temperature of ~900 °C and furnace times up to 25 min [10] and investigated in dry-ice cleaned condition, wide WCRs were observed [10, 11].

For the Al-Si coatings, Laurenz and Ohse [8] show that for 22MnB5 + AS150 hot stamped at 920 °C, the WCR decreases with increase of furnace time (between 6 and 30 min, whereas WCR at 6 min is ~0.5 kA at 15 min is ~0.1 kA and for furnace times of 20 and 30 min, no WCR could be determined) and show an increase of static contact resistance with the furnace time. The authors [9] confirm the observations of lowering of WCR with longer times and also show that higher furnace temperatures lead to lower WCR. They confirm the growth of contact resistance with longer furnace time but find no correlation between the size/position of WCR and measured contact resistance. Ighodaro et al. [7] show that static contact resistances for Al-Si-coated steel are significantly different from peaks of dynamic contact resistances at the beginning of the welding process due to thermal and mechanical influences at the interface and propose to use dynamic contact resistance between the sheet and the electrode to analyze the welding process.

Nevertheless, the static contact resistance is still widely used in industrial applications to anticipate resistance spot weldability. For example, a recommendation of maximal static contact resistance of hot-stamped sheets, measured on a single sheet in compliance with DVS 2929-1 [15], is given in DVS 2935-3 [16]. It is stated that the material is not weldable (it is expected to have a low WCR) when the measured static contact resistance is above 800  $\mu\Omega$  for Al-Si coated and above 1000  $\mu\Omega$  for Zn-coated steels [16]. The present study is aimed to check the correlation of surface layer development in furnace with changes of static and dynamic contact resistance as well as

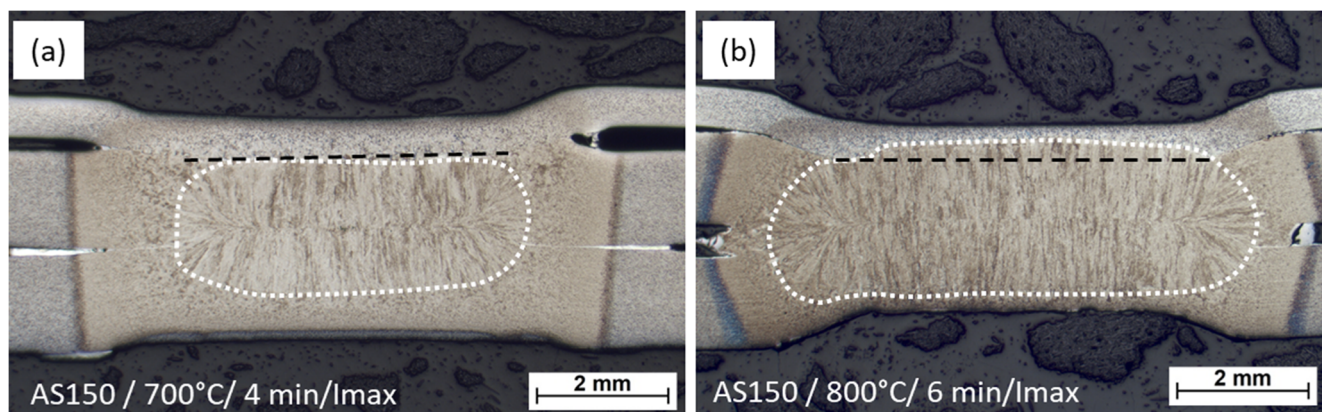


**Fig. 1** Weld nugget in a three-sheet stack-up of a partially hardened 22MnB5 + AS150, described in [14]. **a** Low furnace temperature and short furnace time—no nugget penetration into the thin outer sheet. **b**

Higher furnace temperature and longer furnace time—sufficient nugget penetration into the thin sheet

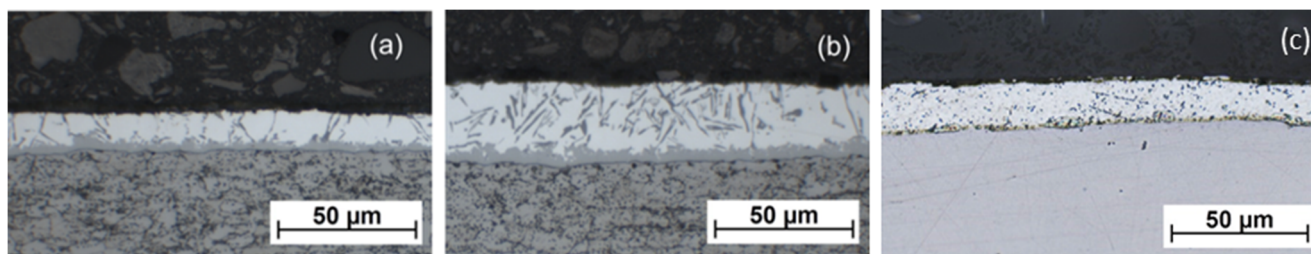


**Fig. 2** Micrographs of test materials in as-delivered condition. 22MnB5 with **a** 80 g/m<sup>2</sup> aluminum-silicon coating and **b** 150 g/m<sup>2</sup> aluminum-silicon coating, both etched with 5% Nital. **c** 22MnB5 with a GA coating 140 g/m<sup>2</sup>, polished

changes of welding current ranges for partially hot-stamped Zn- and Al-Si-coated parts from 22MnB5.

## 2 Experimental procedure

Test material, a commonly used hot stamping steel 22MnB5, was investigated in three surface coating conditions: an Al-Si coating with 80 g/m<sup>2</sup> (sheet thickness 1.45 mm) and 150 g/m<sup>2</sup> as well as a galvanized Zn GI coating with 140 g/m<sup>2</sup> both latter with a sheet thickness of 1.5 mm with coating weights determined by a both sided measurement. Micrographs of the test materials in the as-delivered condition are shown in Fig. 2, chemical composition and mechanical properties are listed in Tables 1 and 2, respectively.

To simulate the partial hot stamping, the variation of furnace temperature and furnace holding times was made, resulting in total of 21 heat treatment conditions for 22MnB5 + AS80, 22 HT conditions for 22MnB5 + AS150, and 12 heat treatment conditions for 22MnB5 + Z140, shown in Table 3. Temperature histories of the sheets in the furnace, measured, using type K thermocouples, welded in the center of the sheet are shown in Fig. 3.

The sheets with dimensions of 300 × 490 mm were cleaned with alcohol, placed into a furnace, which was preheated to a chosen temperature and after the holding

time the sheets were rapidly transported into a flat die and cooled with a cooling rate higher than 27 °C/s and a compression force of 70 kN. After that, specimens for metallographic investigations were extracted from the middle section of a sheet for every HT condition to analyze material and surface layer microstructure, using a precision cutter wet abrasive cutter Buehler Isomet 4000, with subsequent grinding and polishing, removing 0.5 mm from the specimen. Specimens were then etched with a 5% nital solution. Prepared surface layers were photographed at × 500 magnification and for each picture, 10 lines were drawn perpendicular to the coating surface and coating regions (according to [4]) in contact with these lines were measured. A mean value was calculated for each measured layer region and its fraction in the total layer thickness was represented.

Hardness measurements (HV 0,1) were conducted in the cross section of the specimens using a Qness QS60 hardness tester. Five points were measured per HT condition and their mean value was calculated.

Zn-coated sheets for welding experiments underwent manual cleaning by abrasive blasting with glass spheres with diameter of 300–400 µm and air pressure of 4 bar to delete oxide layer. Al-Si-coated sheets were welded in as-hot-stamped condition.

Measurements of static contact resistance were conducted for Al-Si-coated material in as-hot-stamped and Zn sheets in

**Table 1** Chemical composition of test materials in weight percent

	C	Mn	P	S	Si	Al	Ti	B
22MnB5 + AS80	0.22	1.18	0.0109	0.002	0.259	0.03	0.04	0.0034
22MnB5 + AS150	0.23	1.18	0.0109	0.0008	0.254	0.04	0.04	0.0032
22MnB5 + Z140	0.211	1.22	0.013	0.0007	0.202	0.034	0.03	0.0029

**Table 2** Mechanical properties in as-delivered condition

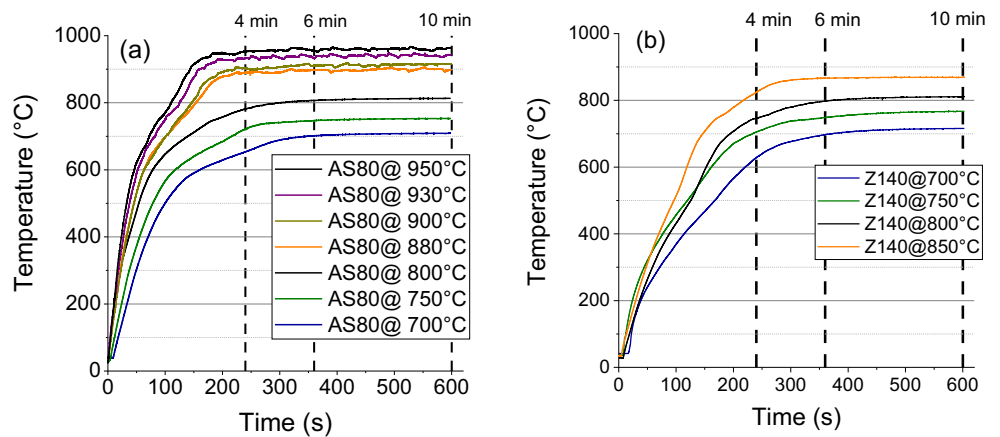
Material	Tensile strength Rm [MPa]	Microhardness [HV 0,1]
22MnB5 + AS80	593 ± 10	189 ± 4
22MnB5 + AS150	565 ± 8	175 ± 11
22MnB5 + Z140	589 ± 7	189 ± 13

**Table 3** Matrix of heat treatments and experiments

Furnace time [min]	22MnB5+AS80 / 22MnB5+AS150							22MnB5+Z140				
	4	R'/W/S		W			W	W	R'/W	W	W	W
6	W	W	W	W	W	S/R'/W	R'/W	W	W	W	W	
10	R'/W		W			W	W/S*	R'/W	W	W	R'/W	
20**	X							W/R'/S	X			
		700	750	800	880	900	930	950	700	750	800	850
<b>Furnace temperature [°C]</b>												

R', dynamic contact resistance measurements (only AS150); S, SEM + EDX for 22MnB5 + AS150; S\*, SEM + EDX for 22MnB5 + AS80; W, WCR determination; \*\* only for 22MnB5 + AS150

**Fig. 3** Temperature histories of specimens in furnace. **a** For 22MnB5 + AS80. **b** For 22MnB5 + Z140

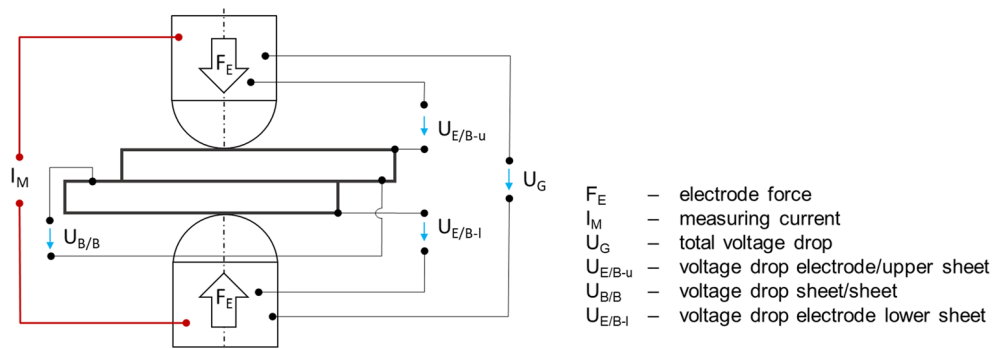


abrasive blasted condition in compliance with a standard DVS 2929-1 [15] on specimens with dimensions 45 × 45 mm.

The measurement procedure, schematically shown in Fig. 4, allowed to measure particular potential drops and thus to calculate corresponding contact resistance components: resistance upper electrode/sheet ( $R_{E/B-u}$ ), resistance between the two sheets ( $R_{B/B}$ ), and resistance between the lower electrode/sheet ( $R_{E/B-l}$ ). Total contact resistance ( $R_C$ ) was also measured

and compared to the sum of partial resistances to verify the measurement procedure. Direct current  $I_M$  of 10 A and pneumatically applied electrode force  $F_E$  of 3.5 kN were used. Three measurements per HT condition were conducted using dome shaped electrode tips F0-16-20-8 DIN EIN ISO 5821:2011 Fig. 5a. To compare measurement results with the requirements of [16], a sum of contact resistances electrode-sheet  $\Sigma R_{E/B}$  was calculated (1):

**Fig. 4** Schema of contact resistance measurement in compliance with DVS 2929-1 [15]



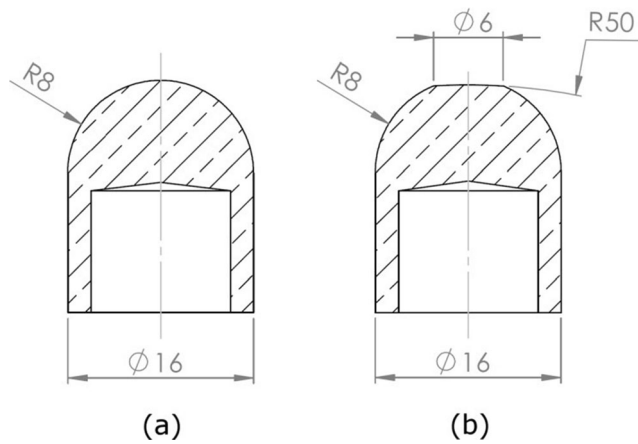


**Fig. 5** Schematic drawing of the cross section of electrode tips. **a** Electrode tips F0-16-20-8 DIN EIN ISO 5821:2011, used for contact resistance measurements. **b** Electrode tips F1-16-20-8-50-6 DIN EIN ISO 5821:2011, used for welding experiments

$$\sum R_{E/B} = R_{E/B-u} + R_{E/B-l} \tag{1}$$

Resistance spot welding was performed using a stationary welding system in C construction with a 1000 Hz medium frequency inverter (MFDC) from Nimak with a magneticDrive® force module. The electrode force is applied, using an electromagnet and is being held constant during the welding process, as described in [9].

Welding parameters, chosen from SEP 1220-2 [17] for coated sheets in the thickness range between 1.35 and 1.64 mm, are listed in Table 4. Welds were made with electrode tips F1-16-20-8-50-6 DIN EIN ISO 5821:2011 (Fig. 5b) made from CuCr1Zr. According to SEP1220-2, the electrode tips were milled before determining each welding current range using a handheld electrode milling device EF 810-E1 from SVS-Schweißtechnik with a milling inset to achieve the electrode geometry, depicted in Fig. 5b. Welding current, voltage, electrode force, and displacement were monitored for each weld, using a HKS WeldQAS measuring device.

To determine the welding current range (WCR) in compliance with SEP1220-2 [17], welding current was varied. Starting from 4.0 kA, two welds for each welding current setting were made. If at least one of them was welded without the expulsion, welding current was increased by 0.2 kA and two welds were made with the new welding current. This routine was repeated until welding current setting was reached, at which both welds had an expulsion ( $I_u$ ). After that welding current was decreased with a step of 0.1 kA until

three subsequent welds at the same welding current were welded without an expulsion. This current ( $I_{max}$ ) determines the upper limit of the WCR. The lower limit of the welding current range is the lowest setting of welding current, at which the minimum weld diameter  $d_{w_{min}}$  of  $4\sqrt{t}$ , where  $t$  is the sheet thickness, is reached with certain reproducibility. To determine it, welded specimens, starting at the welding current of 4.0 kA underwent the chisel test until weld diameter of both welds at the same welding current was above the  $d_{w_{min}}$ . Three subsequent welds were made at this welding current, destroyed using a chisel test and their weld diameters were measured. If the  $d_w$  for at least one of them was below  $d_{w_{min}}$ , welding current was increased by 0.1 kA and another three welds were made and measured. The procedure was repeated until a welding current ( $I_{min}$ ) was reached, at which weld diameters for all three measured specimens were larger than  $d_{w_{min}}$ . In the region between  $I_{min}$  and  $I_{max}$  (WCR), weld diameter is sufficient and the expulsion is improbable, in the region between  $I_{max}$  and  $I_u$  (unstable region), both expulsion and expulsion free welds may be produced. At welding currents above  $I_u$ , a very high probability of expulsion exists.

The welding current ranges, determined under the standard procedure of SEP 1220-2, can be used to quantify and compare the joinability of different materials and material conditions with wider WCR corresponding to a higher joinability of the material [17].

Measurements of total dynamic resistance in the welding process were conducted, using a HKS-WeldQAS measurement system for HT conditions, marked in Table 3. To make a comparison between measurements possible, they were conducted at  $I_{min}$ , resulting in equal weld diameter for all HT conditions except AS150 at 950 °C with the furnace time of 20 min, where no WCR could be determined because of expulsion already at 4 kA. For this material condition, dynamic resistance was measured for the welding current of 4 kA. In total, three measurements per HT conditions were conducted and averaged.

### 3 Results and discussion

#### 3.1 Material properties

Three grades of material strength were generated by variation of furnace temperature and time, as can be seen in Fig. 6. At low furnace temperature of 700 °C, all three test materials had

**Table 4** Welding parameters in compliance with SEP 1220-2 [17]

Squeeze time $t_s$ [ms]	Welding current $I_w$ [kA]	Welding time $t_w$ [ms]	Electrode force $F$ [kN]	Holding time $t_h$ [ms]
200	4.0, $I_u$	380	4.5	300

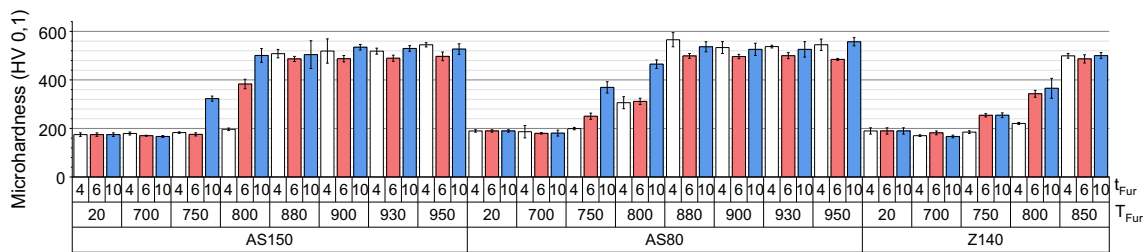


**Fig. 6** Evolution of material hardness with furnace time and temperature

low hardness regardless of the furnace time, corresponding to the ferritic-pearlitic microstructure. For high furnace temperatures, beginning with 850 °C for Zn and 880 °C for Al-Si-coated 22MnB5, high hardness was measured, corresponding

to full austenitization of the material in the furnace and its subsequent transition to martensite. No significant influence of the furnace time on the material properties was observed at temperatures above 850 °C.

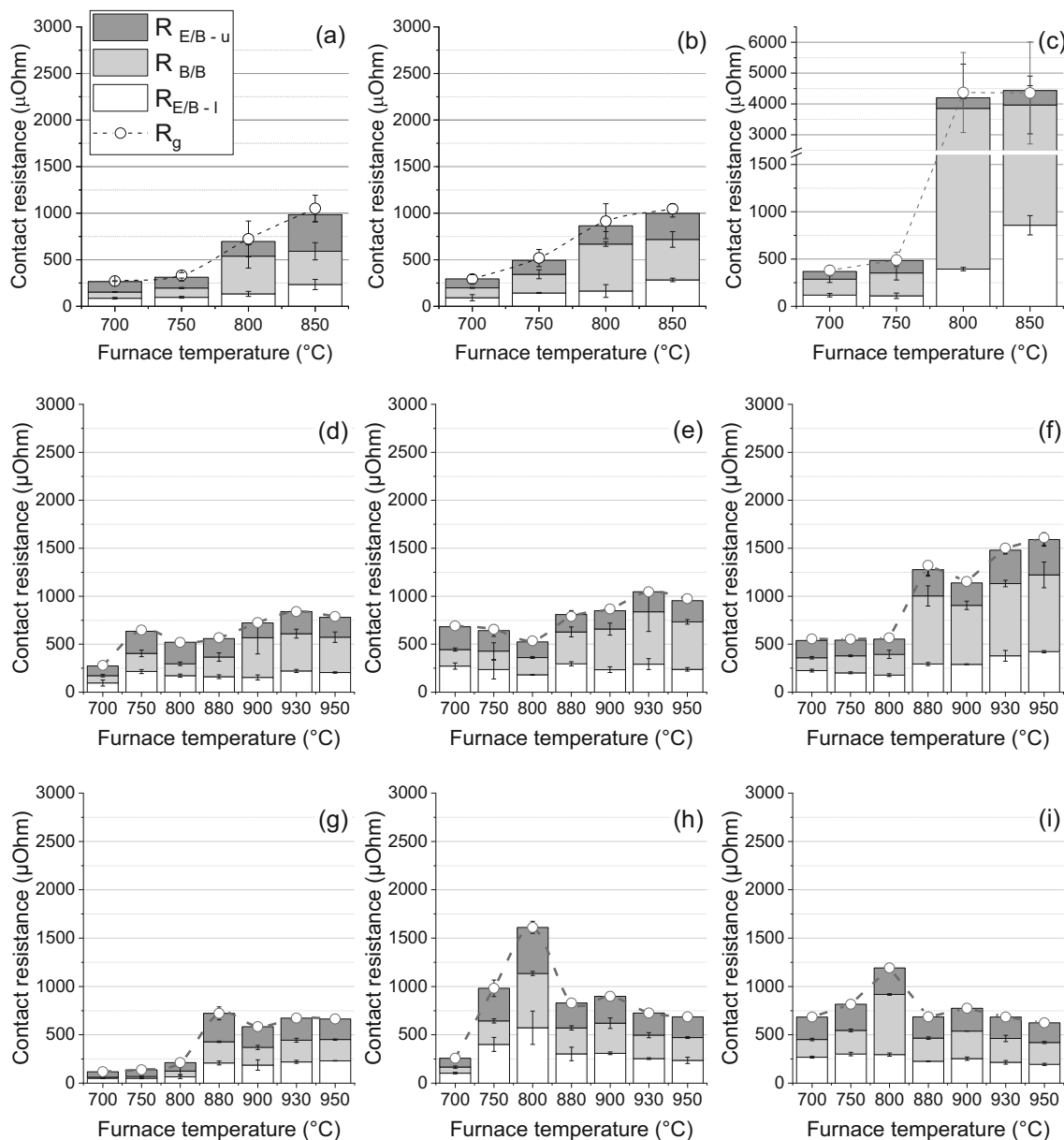


**Fig. 7** Measured contact resistance for different heat-treated conditions. **a–c** 22MnB5 with Zn coating. **d–f** 22MnB5 with Al-Si coating 80 g/m<sup>2</sup>. **g–i** 22MnB5 with Al-Si coating 150 g/m<sup>2</sup>. **a, d, g** Furnace time 4 min. **b, e, h** Furnace time 6 min. **c, f, i** Furnace time 10 min

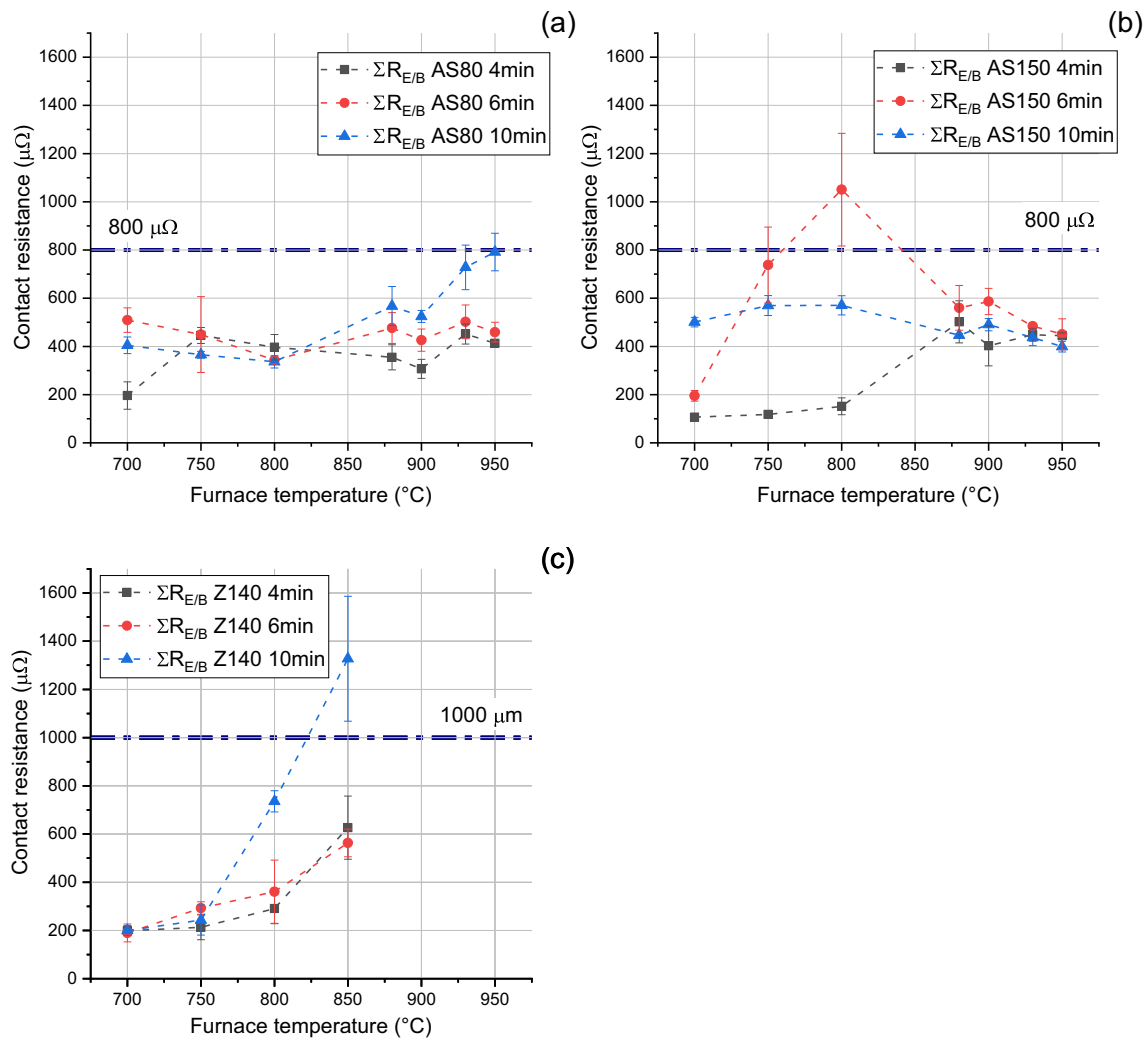


**Fig. 8** Sum of static contact resistances between electrodes and sheets  $\Sigma R_{E/B}$ . **a** For 22MnB5 + AS80. **b** For 22MnB5 + AS150. **c** For 22MnB5 + Z140

A transition region in which material did not undergo full austenitization and which after cooling contains martensite, rest ferrite, and bainite [13] was observed at 750  $^{\circ}C$  and

800  $^{\circ}C$ . In this region, furnace time had a significant influence on material hardness, with longer soaking times leading to higher material hardness.

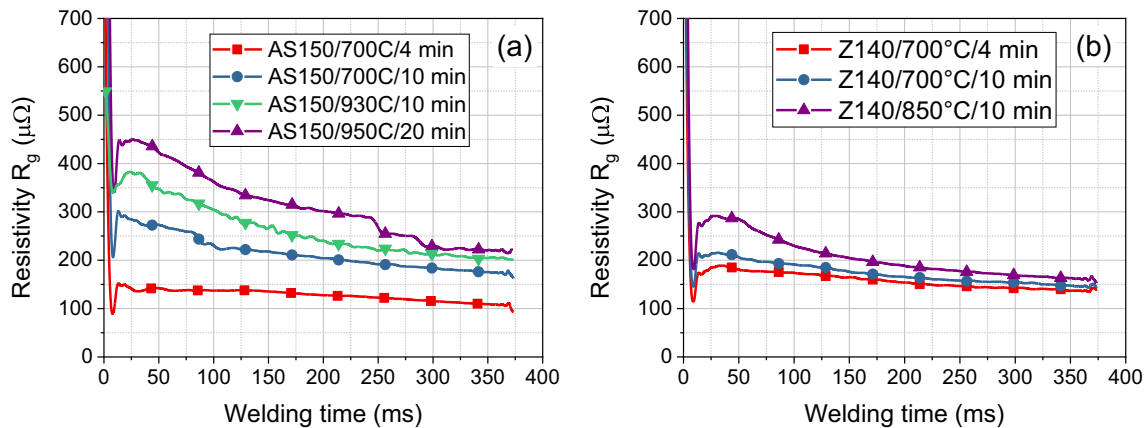


**Fig. 9** Dynamic total resistances. **a** For 22MnB5 + AS150. **b** For 22MnB5 + Z140

### 3.2 Contact resistance

For 22MnB5 + Z140, contact resistance shows a clear trend of increasing with increasing furnace temperature and time due to formation of resistive Fe-rich phases in the coating [6, 18]. At furnace times of 4 and 6 min (Fig. 7a and b respectively), the total contact resistance is below 1000  $\mu\Omega$ . For furnace time of 10 min and temperatures of 800 °C and 850 °C, it reaches ~ 4100  $\mu\Omega$  and ~ 4300  $\mu\Omega$  respectively and shows high scattering, as can be seen in Fig. 7c. This might be caused by formation of a more consistent oxide layer at higher temperatures and soaking times [6], which cannot be fully removed by abrasive blasting; however, further investigations are required to confirm this suggestion. For all other furnace temperatures and times, a proportional increase of all three resistance components: resistance upper electrode/sheet ( $R_{E/B-u}$ ), resistance between the two sheets ( $R_{B/B}$ ), and resistance between the lower electrode/sheet ( $R_{E/B-l}$ ) was observed with temperature increase, except the holding time of 10 min at 800 °C and 850 °C. For these conditions, the contact resistance between the two sheets ( $R_{B/B}$ ) was much higher than that of resistance between electrode and sheet.

Measured contact resistances for 22MnB5 + AS80 follow a similar trend, with higher furnace temperatures and times corresponding to higher measured contact resistance. Proportional growth of all three resistance components is observed. However, the growth of contact resistance with the furnace temperature and time is less pronounced (confirming the observations of [8]), compared to Zn-coated steel.

For 22MnB5 + AS150, measured contact resistances have shown a good correlation with the layer development at lower furnace temperatures and times (700, 750, 800 °C at 4 min and 700 °C at 6 min). Low contact resistances were measured for layer conditions, where metallic Al-Si coating (with low

hardness and resistivity) is present on the specimen surface. Further increase of furnace time and temperature leads to a significant increase in contact resistance. For furnace times 6 and 10 min, a peak in contact resistance was observed at 800 °C, for 4 min the peak moved to 880 °C. This increase might be caused by the formation of thin Al- and Si-oxide layers on the specimen surface, reported in [18]; however, it is still unclear why the described phenomenon was not observed at higher furnace temperatures. For furnace temperatures above 900 °C for furnace time of 4 min, only slight increase in contact resistance is observed, for 6 and 10 min, the contact resistances are decreasing with increasing furnace temperature.

Development of contact resistance between electrodes and sheets for both Zn and Al-Si-coated steels are presented in Fig. 8. For 22MnB5 + Z140,  $\Sigma R_{E/B}$  was higher than the recommended threshold of 1000  $\mu\Omega$  only for one heat-treated condition—850 °C at 10 min. For 22MnB5 + AS150,  $\Sigma R_{E/B}$  exceeded the recommended maximal threshold of 800  $\mu\Omega$  only for one HT condition with 800 °C at 6 min and for 22MnB5 + AS80 resistance between electrode and sheet lied below 800  $\mu\Omega$  for all heat-treated conditions (the highest resistance  $\Sigma R_{E/B}$  792  $\mu\Omega$  for 950 °C at 10 min).

### 3.3 Dynamic resistance measurements

Measurements of dynamic resistance in the welding process between the electrodes ( $R_g$ ) were conducted for AS150 and Z140 in HT conditions, representing different groups of surface layer development, as described in Sections 3.4 and 3.5 of this paper. For AS150, specimens heat-treated at 700 °C with 4 min (metallic Al-Si regions in layer are still present), and 10 min (layer consists of intermetallic phases), as well as the representative of the group where resistive intermetallic phases (regions B, C, and E) are present with the fraction between 51 and 84%—950 °C/10 min and a group for which the layer consists mostly of resistive intermetallics (more than 84%)—20 min at 950 °C. For 22MnB5 + Z140, the HT conditions with low measured contact resistance (4 and 10 min at 700 °C) were compared to the condition where an extremely high contact resistance was measured—10 min at 850 °C.

Higher dynamic resistance was measured for specimens with longer furnace times and higher furnace temperatures for both coatings, whereas AS150-coated specimens had higher resistance, compared to Z140 (except specimens with 4 min at 700 °C), as can be seen in Fig. 9. Static contact resistance measurements show an opposite trend.

Dynamic resistances drop drastically in the first milliseconds of the welding process as described in [7, 19]. A peak of dynamic resistance in the first 20–30 milliseconds is associated with growth of total resistance because of increase of bulk resistance due to heating; the further drop is explained by nugget growth [19]. Heat treatment condition with a higher

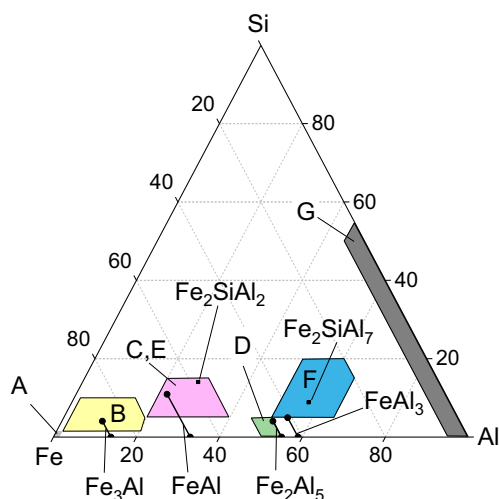


**Fig. 10** Regions of the Al-Si layer and chemical composition of common Al-Si-Fe phases after [4] (in wt.%)

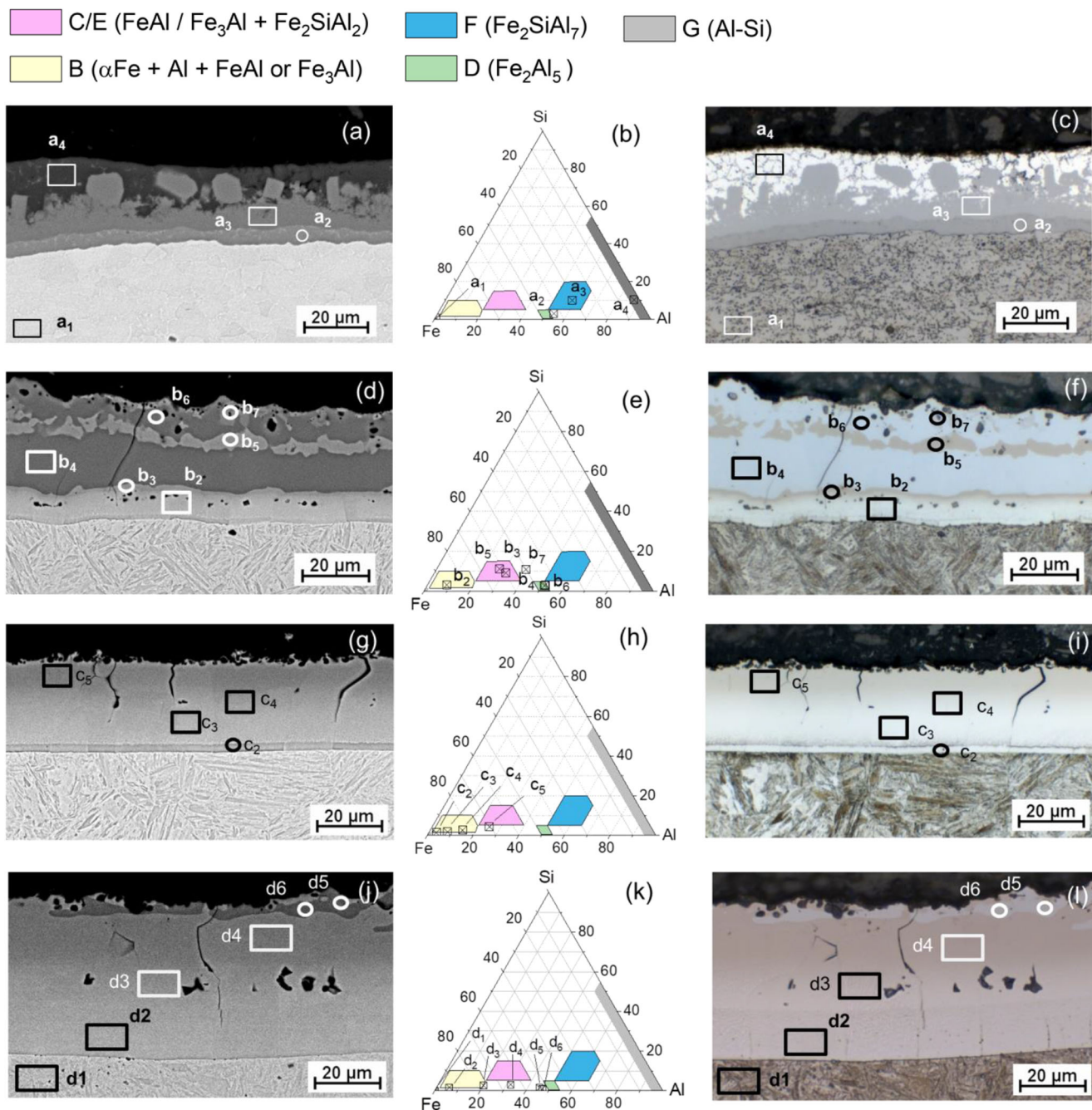


**Fig. 11** BSE (a, d, g, j) and light microscopic (c, f, i, l) images with marked EDS measurements. b, e, h, k Chemical compositions of the measured spots/surfaces and layer regions after [4]. a–c 22MnB5 +

AS150 700 °C/4 min. d–f 22MnB5 + AS150 930 °C/6 min. g–i 22MnB5 + AS80 950 °C/10 min. j–l 22MnB5 + AS150 930 °C/20 min

fraction of resistive phases shows a larger drop of resistance after first 30 ms of welding time, which allows to assume a more intensive nugget growth.

For Zn specimens, a correlation between the static and dynamic resistance may be suggested, with higher measured static contact resistance corresponding higher dynamic resistance, for 22MnB5 + AS 150 no such correlation can be seen.

### 3.4 Surface layer development of 22MnB5 + AS

The description of surface layer development was made, based on investigations of Jenner et al. [4]. The authors suggest a classification of 7 regions in the Al-Si-coated 22MnB5 steel heat-treated at 920 °C with different furnace times, using EDS measurements to define chemical composition field for each region (Fig. 10) and describe possible phases. The

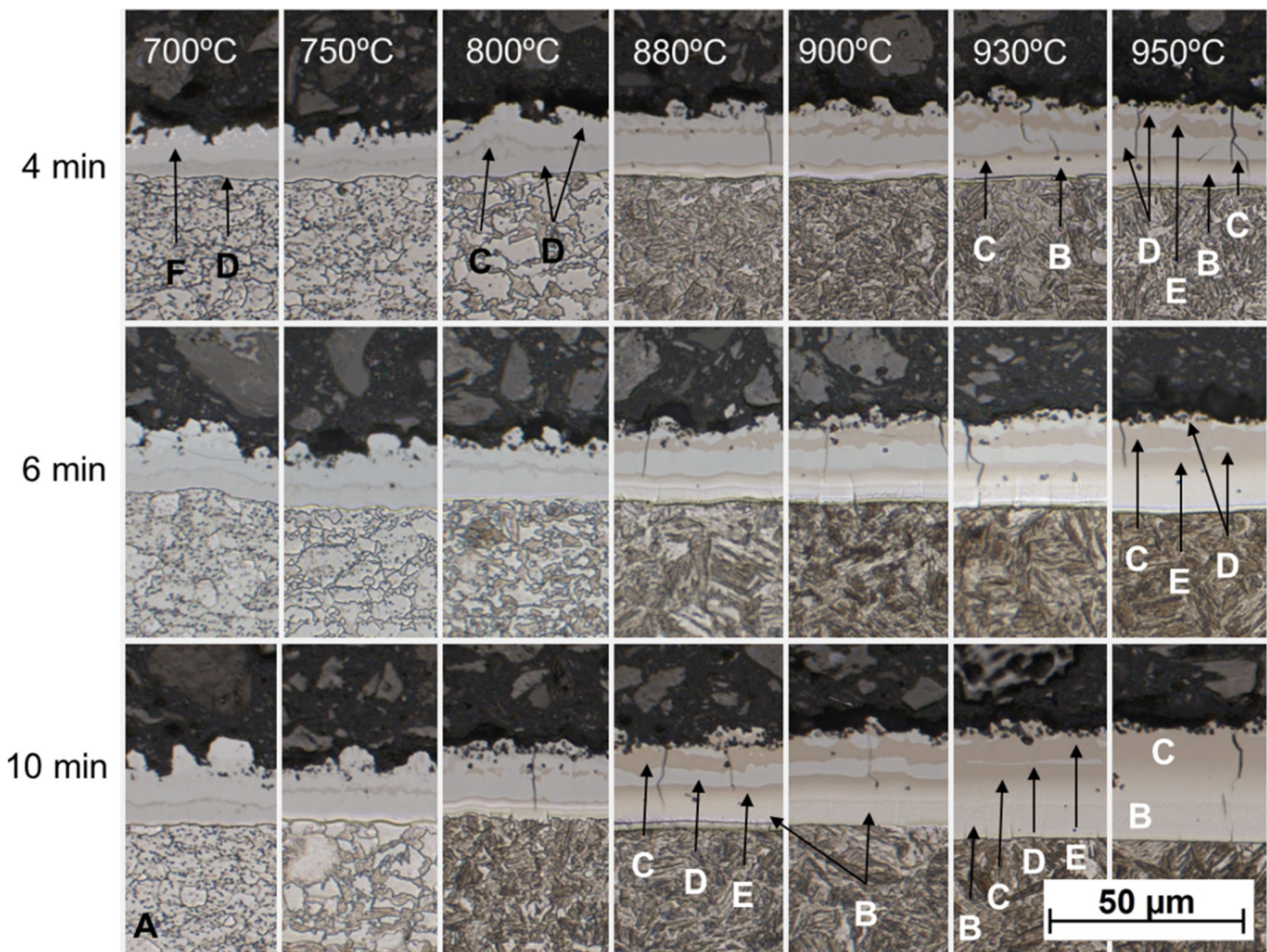


**Fig. 12** Cross sections of surface layer for 22MnB5 + AS80 in investigated HT conditions with marked layer regions after [4]

regions are labeled from A—the steel substrate to G—metallic Al-Si coating according to their position in the layer and development time.

In the current investigations, the proposed classification system, as well as identification of phases, was used to describe the layers, shown in Fig. 3. For that, a comparison of the SEM images and EDX measurements with the light microscopy images was conducted, as shown in Fig. 11.

For the heat-treated condition with  $T_{\text{fur}} 700\text{ }^{\circ}\text{C}$ ,  $t_{\text{fur}} 4\text{ min}$  (Fig. 11a–c), four regions could be identified: steel substrate A ( $a_1$ ), an intermetallic layer D ( $a_2$ ), intermetallic layer F ( $a_3$ ), and the G layer—metallic Al-Si coating. Measured aluminum content in the spot  $a_2$  is slightly higher than that, given by Jenner et al. (Fig. 11c). It can be explained by inhomogeneous Al distribution in the region. The backscattered electron (BSE) picture (Fig. 11a) shows differences in gray scales with darker regions richer in light elements (Al and Si). All identified layers are well visible in the LM image (Fig. 11b).

Figure 11d–f shows the layer condition with  $T_{\text{fur}} 930\text{ }^{\circ}\text{C}$ ,  $t_{\text{fur}} 6\text{ min}$ . In this condition, a layer structure with multiple

intermetallic regions was identified. Assignment of layers according to the EDX measurements (Fig. 11d, e) leads us to the following layer structure: area  $b_2$  corresponds to the region B, followed by regions C (spot  $b_3$ ) and D ( $b_4$  and  $b_6$ ) with region E ( $b_5$ ). This region is inhomogeneous, ( $b_7$ ) marks an “isle” of region E, surrounded by region D. Its measured chemical composition does not correspond the region E after Jenner et al. ( $b_7$  has higher Al content), which can be caused by the fact that the EDX-measured volume includes the surrounding D layer with higher Al content because of the small size of the “island” of only several micrometers. Considering lighter in gray scales in the BSE image and brown color of the “isle” in the LM image, contrasting with the surrounding material, as well as its chemical composition with more Al and Si, compared to region D, it is allocated as part of the E region.

Figure 11g–i shows the conducted measurements for 22MnB5 + AS80 with  $T_{\text{fur}} 950\text{ }^{\circ}\text{C}$ ,  $t_{\text{fur}} 10\text{ min}$ . Lighter regions of the layer (light-gray BSE, yellow-gray LM) can be allocated as region B according to their chemical composition;

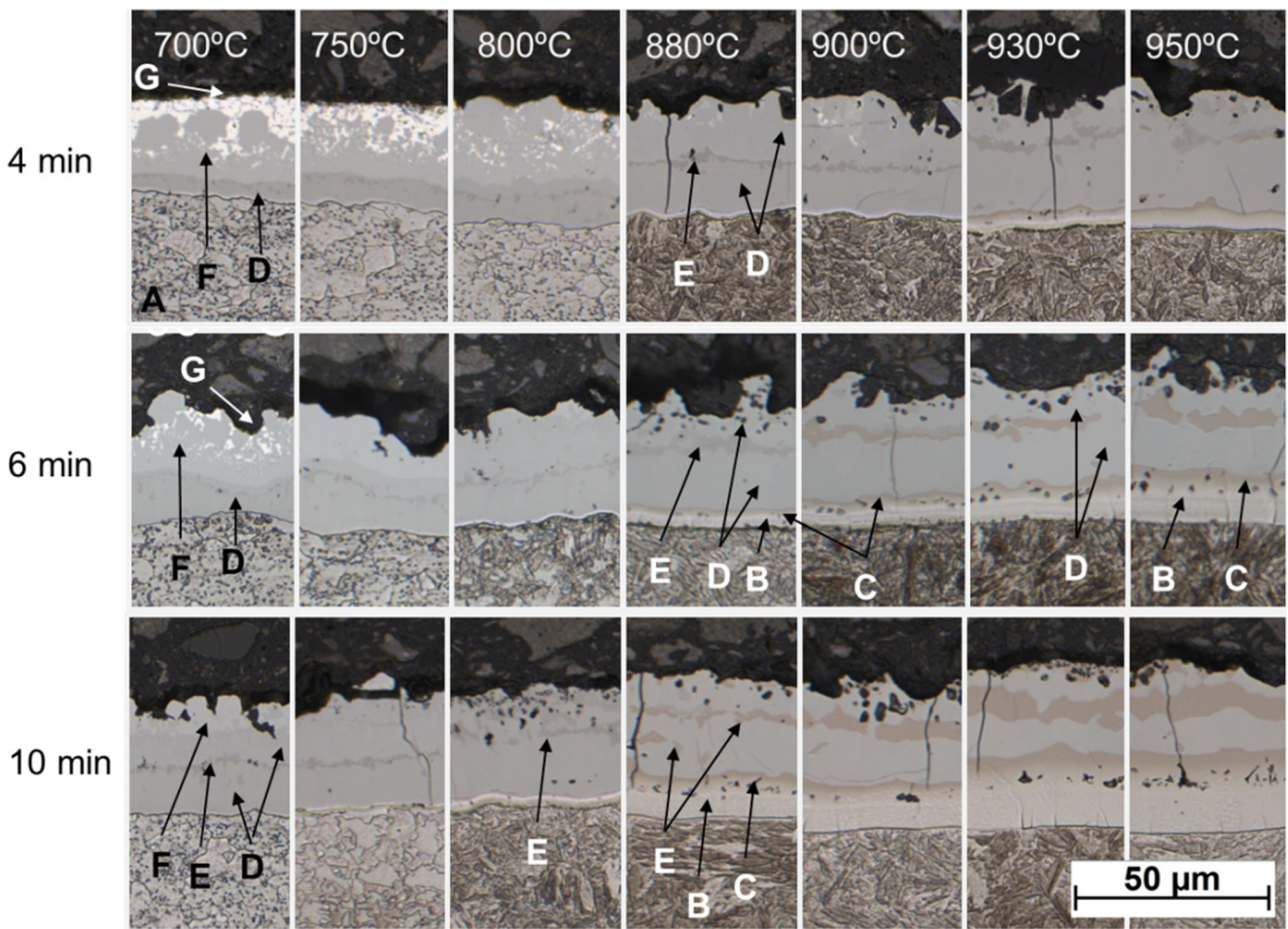


Fig. 13 Cross sections of surface layer for 22MnB5 + AS150 in investigated HT conditions with marked layer regions after [4]

measured area  $c_5$  (dark-gray BSE/light-brown LM) is considered as the layer C.

A direct comparison between light microscopic and BSE image for 22MnB5 + AS150 heat treated for 20 min at 950 °C is shown in Fig. 11j–l. The layer is almost completely diffused

and consists of regions B with 58% (d2–d3) and C/E 31% of the total layer thickness (d4) only a small fraction of region D is present in form of “isles” in the surrounding region C/E.

Using the allocated layer regions, measurements of the thickness of different layer regions were conducted, as

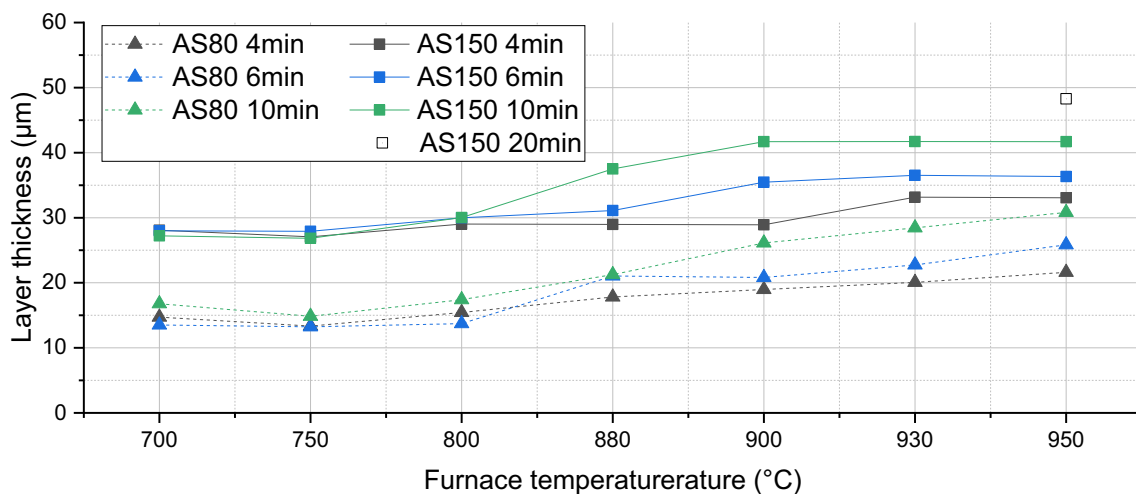
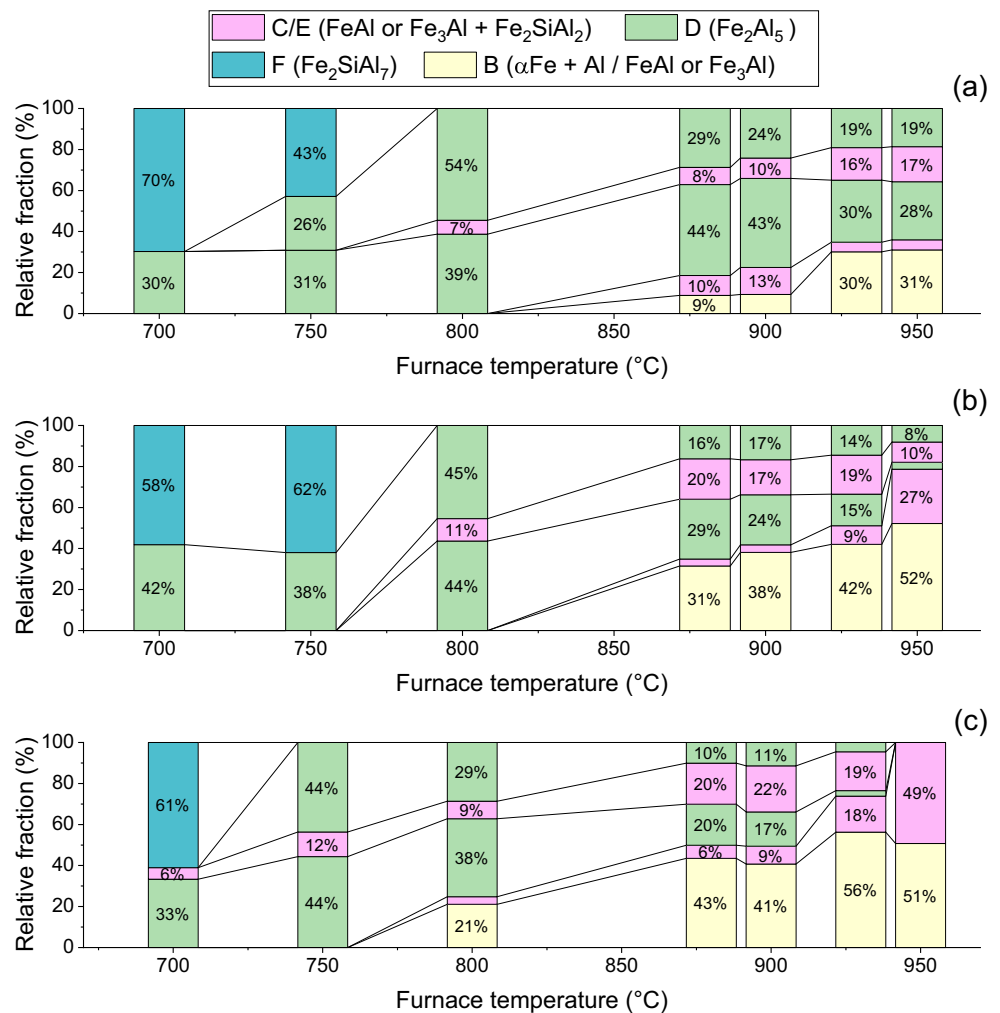


Fig. 14 Change of the total layer thickness with furnace temperature for the investigated furnace times

**Fig. 15** Al-Si layer (80 g/m<sup>2</sup>) development in furnace depending on furnace temperature for the investigated furnace times. **a** 4 min. **b** 6 min. **c** 10 min



described earlier, using light-microscopic images. Layer regions are marked in LM cross section micrographs for 22MnB5 + AS80 (Fig. 12) and + AS150 (Fig. 13).

Change of the total layer thickness with furnace temperature is shown in Fig. 14; development of individual layer regions with temperature and time is visualized in Fig. 15 for 22MnB5 + AS80 and Fig. 16 for 22MnB5 + AS150.

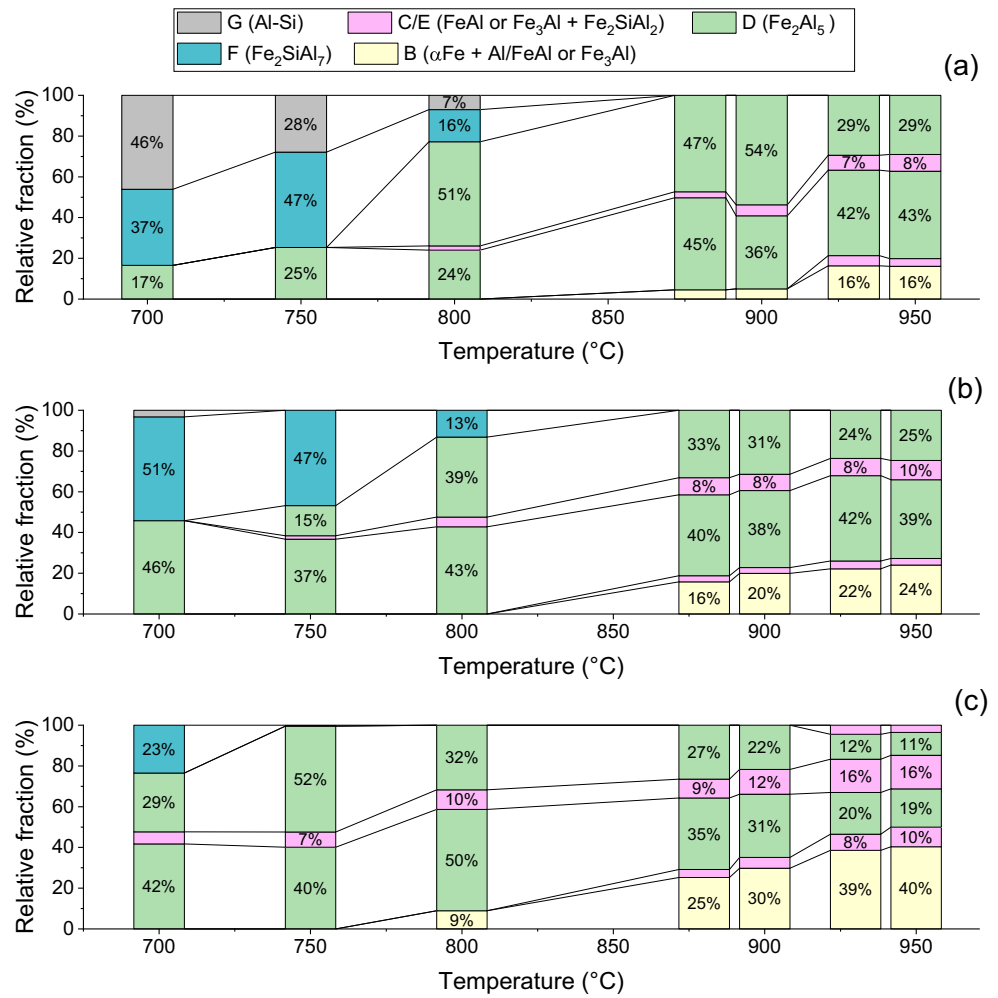
At the beginning of the heat treatment in the furnace, the Al-Si coating layer consists of metallic Al-Si (region G) with minor intermetallic phases, as was previously described. The development of the layer is controlled by diffusion process and therefore depends on layer thickness, as well as furnace temperature and holding times. The thinner the layer, the less time at a given temperature is needed for the diffusion to take place. Higher holding temperatures lead to acceleration of diffusion processes in the layer [20]. For AS150, the region G—metallic Al-Si coating can be found at 700 °C and 750 °C with furnace times of 4 min, some of it still visible at 800 °C; at 6 min minor amount of G region is still present at 700 °C with a furnace time of 6 min. The rest of the coating at these temperatures consists of regions F—mainly ternary

intermetallic phase Fe<sub>2</sub>SiAl<sub>7</sub> and D—mainly intermetallic compound Fe<sub>2</sub>Al<sub>5</sub>. For AS80, marginally small amount of region G is still present at 700 °C and 4 min furnace time, but at 6 min, it is completely transformed into the F region.

For both coatings, the development of region E—a mixture of ternary intermetallic Fe<sub>2</sub>SiAl<sub>2</sub> with binary phase FeAl or Fe<sub>3</sub>Al is observed beginning with 700 °C and 10 min. According to [4, 18], it is formed because with enrichment of the F region with Fe and its transformation into the Fe<sub>2</sub>Al<sub>5</sub> (region D) with lower Si solubility. The rest Si forms the Fe<sub>2</sub>SiAl<sub>2</sub> phase in the middle of the Fe<sub>2</sub>Al<sub>5</sub>. Growth of the E region is observed with higher furnace temperatures and proceeding furnace time.

Beginning with 800 °C and 10 min, regions B (for both coatings) and C (for AS150 the observed beginning with 880 °C) are formed at the interface between the substrate and the Al-rich coating. Region C has the same phase composition as the region E. Region B, the interdiffusion region between the Al-Si coating and steel consists of α-Fe and ~ 10 wt.% (~ 15 at. %) Al with the possible presence of the Fe-rich intermetallic phase Fe<sub>3</sub>Al [4]. With higher temperatures and furnace times,

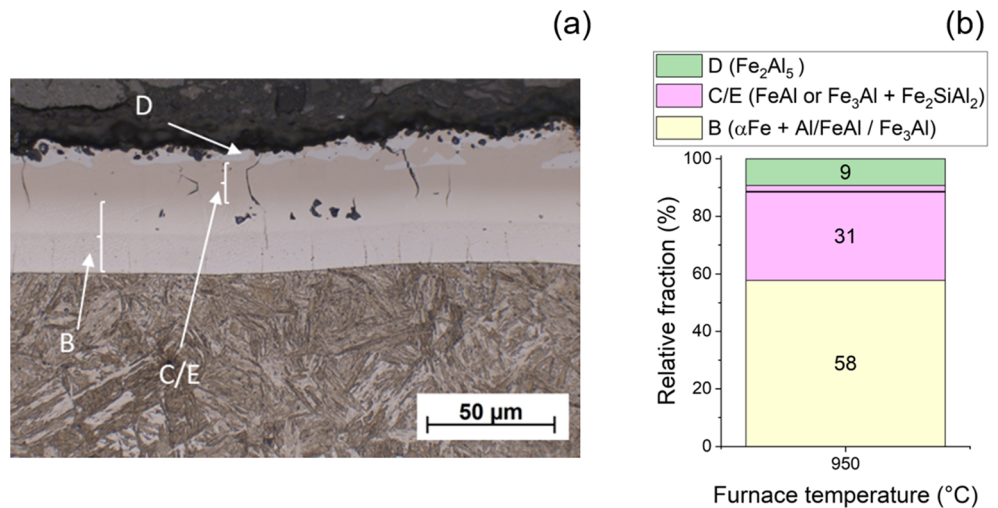
**Fig. 16** Al-Si layer (150 g/m<sup>2</sup>) development in furnace depending on furnace temperature for the investigated furnace times. **a** 4 min. **b** 6 min. **c** 10 min



growth of regions E, C, and B and simultaneous reduction of the D region is observed due to Fe-enrichment of the coating. For furnace time of 10 min at 950 °C, the layer for AS80 consists of two regions: B (51%) and C (49%), for

22MnB5 + AS150 due to its higher thickness, decent amount (30%) of the D region is still present in the layer. The rest of the layer consists of regions B, C, and E. For the holding time of 20 min at 950 °C (Fig. 17), the surface layer condition for

**Fig. 17** **a** Cross section of the layer. **b** Relative fraction of layer regions for the HT condition AS150/950 °C/20 min



22MnB5 + AS150 is comparable to the layer condition of 22MnB5 + AS80. The layer for AS150 is thicker (48.3  $\mu\text{m}$ ), in comparison to AS80 (31  $\mu\text{m}$ ) (Fig. 13), but the phase composition is close, with regions B and C/E occupying 91% of the layer for AS150 (Fig. 16a) and 99% for AS80 (Fig. 15c).

According to [21, 22], the resistivity of the Fe-Al system at room temperature strongly increases with increasing of Al content (resistivity peak of 165  $\mu\Omega\text{ cm}$  at approximately 33 at. % Al) and shows a steep decrease with further Al additions. Interpolating these results with the chemical compositions of individual layer regions from [4] (considering only Fe and Al contents) as shown in Fig. 18 leads to the suggestion that layers B and C/E have a much higher resistivity, compared to the steel substrate ( $\sim 25\ \mu\Omega\text{ cm}$  [23]) as well as Al-rich layers G, F, and D.

### 3.5 Welding current ranges

Significant differences in welding current range size between 22MnB5 with Zn and Al-Si coating were observed (Fig. 19). For Zn coating at furnace times of 4 and 6 min, no shift of welding current ranges towards lower welding currents is evident, although an apparent growth of static contact resistance with increasing furnace temperature and time is present. The reduction of welding current range and its shift towards lower currents was registered only at 10 min furnace time and furnace temperatures of 800 and 850  $^{\circ}\text{C}$ . Despite large reduction of welding current range, the determined WCR for 800  $^{\circ}\text{C}$  was 1.8 kA and for 850  $^{\circ}\text{C}$ —1.1 kA, which is slightly below the recommended WCR of 1.2 kA [25]. In the HT condition of 800  $^{\circ}\text{C}/10\text{ min}$ , the sum of the static contact resistances between electrode and sheet ( $\Sigma R_{E/B} = 734\ \mu\Omega$ ) did not exceed the threshold of 1000  $\mu\Omega$ , for 850  $^{\circ}\text{C}/10\text{ min}$  ( $\Sigma R_{E/B} = 1037\ \mu\Omega$ ), the threshold was exceeded.

For 22MnB5 + AS, a clear trend of shifting of the WCR towards lower welding current and simultaneously its reduction with an increase of furnace temperature and time is observed. The trend is more pronounced for 22MnB5 + AS80.

No correlation of welding current range with the measured static contact resistance for both Al-Si coatings could be identified. For example, for 22MnB5 + AS150, furnace temperature/time combinations of 800  $^{\circ}\text{C}/6\text{ min}$  and 800  $^{\circ}\text{C}/10\text{ min}$  with highest measured contact resistances (total resistance  $R_G$ —1611 and 1191  $\mu\Omega$ ,  $\Sigma R_{E/B}$ —738 and 1050  $\mu\Omega$ , respectively) still have a WCR of correspondingly 2.0 and 2.4 kA. For the HT condition with significantly lower total contact resistances (e.g.,  $R_G$  of 686  $\mu\Omega$  and  $\Sigma R_{E/B}$  of 450  $\mu\Omega$  for 950  $^{\circ}\text{C}/6\text{ min}$ ), the WCR is much lower—1.2 kA, and for the HT condition 950  $^{\circ}\text{C}/10\text{ min}$  with the  $R_G$  of 625  $\mu\Omega/\Sigma R_{E/B}$  of 450  $\mu\Omega$ , the WCR is only 0.4 kA.

For AS80,  $\Sigma R_{E/B}$  does not exceed the recommended threshold of 800  $\mu\Omega$  in any HT condition; however, a massive change in the WCR is observed.

For 22MnB5 + AS150, heat treated for 20 min at 950  $^{\circ}\text{C}$  no welding current range could be determined; expulsions were registered already at 4.0 kA before  $I_{\text{min}}$  was reached.

A correlation between layer development and the welding current range can be clearly seen.

According to simulation results from [19], conducted for uncoated low alloyed steels, the contact resistance is actively influencing the heat generation only during first few milliseconds of the welding time, in which the peak of current density and peak of heat generation are located in the zone with high contact resistance. After a fully contacted area between the sheets (corona bond) is formed in which resistance is governed by temperature-dependent material resistivity, peak of current density relocates into this area, leading to more active heat generation in it. Heat is also generated in the middle of the weld; it exceeds melting temperature and weld

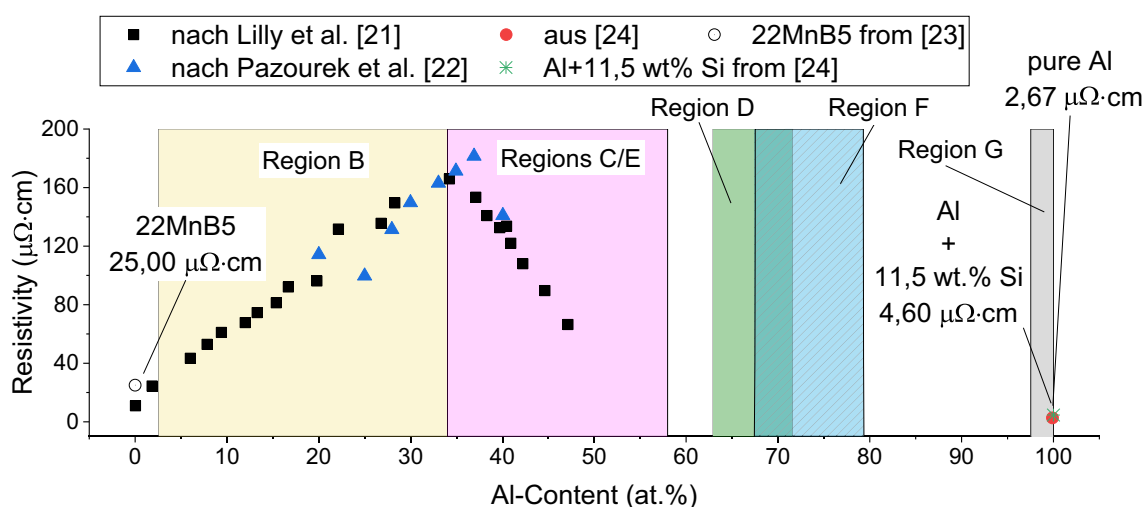
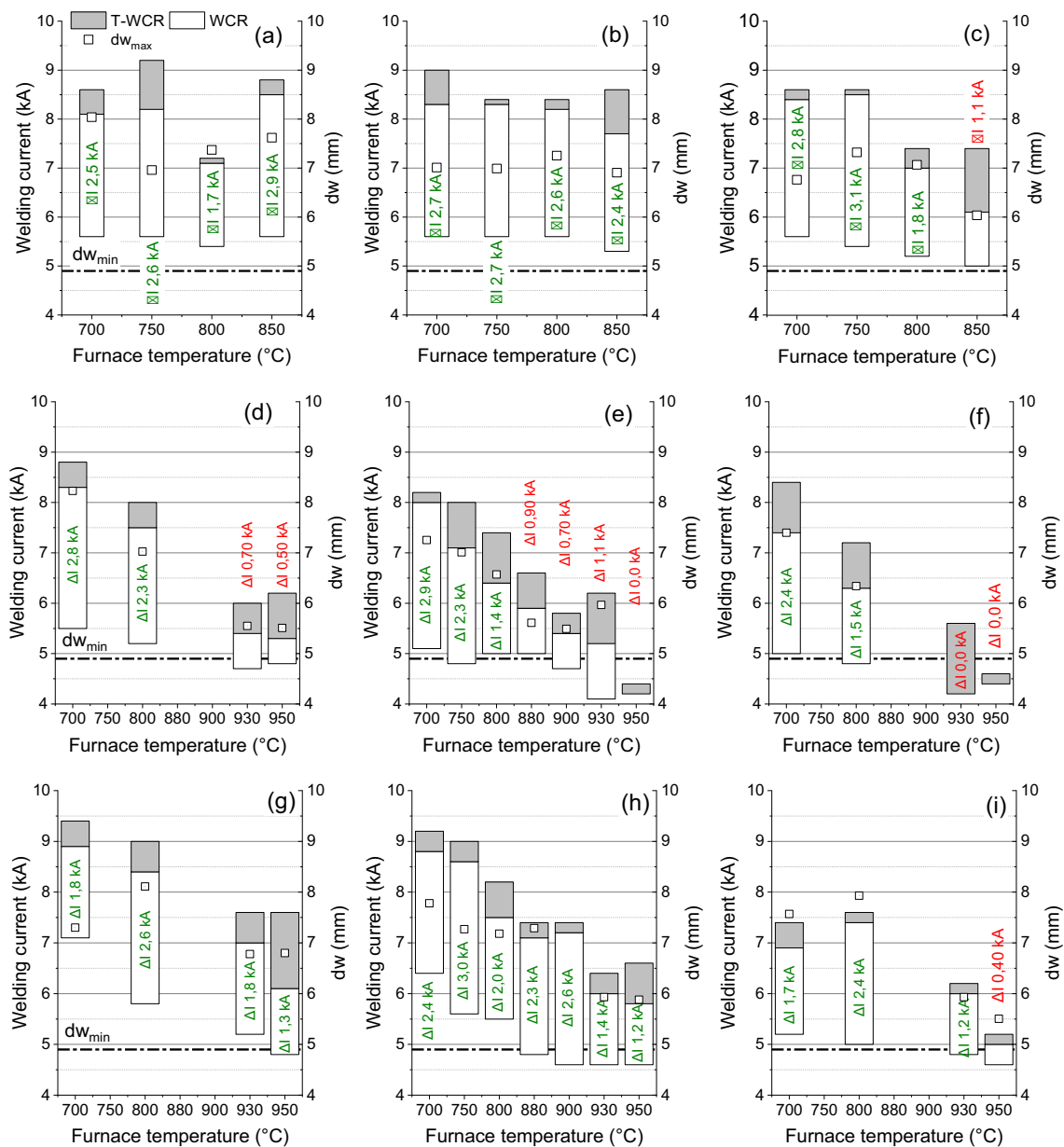


Fig. 18 Resistivity of binary Fe-Al alloys, depending on the Al content after [21–24] with marked layer regions after [4]



**Fig. 19** Welding current ranges for **a–c** 22MnB5 + Z140; **d–f** 22MnB5 + AS80; and **g–i** 22MnB5 + AS150 with different furnace times. **a, d, g** Furnace time 4 min. **b, e, h** Furnace time 6 min. **c, f, i** Furnace time 10 min

nugget is formed. With nugget growth, a constant increase of the corona bond area is observed; current density peak and peak of heat generation are moving further from the nugget center, but are still located in the corona bond.

When low-resistive metallic Al-Si (region G) is present in the layer, lower resistance at the beginning of the welding process leads to lower heat generation; the WCR is reduced and shifted towards higher welding currents. In case of a two-sheet stack-up, only a slight reduction of the WCR was observed; however, low resistance at the interface may influence the nugget development and therefore be critical in case of three-sheet stack-ups with a thin outer sheet, where nugget penetration into the thin sheet is of great significance.

Presence of resistive intermetallic layers in the corona bond leads to more intense heat generation in this region and may also cause a redistribution of welding current, leading to higher current density in the middle of the weld and as a consequence to higher heat generation in it. Resistive and therefore less heat conductive layers at the interface between the electrode and sheet lead to more intense heat generation at the interface and worse cooling of the weld, as suggested in [26].

The described effects cause a more rapid nugget growth compared to the growth of the corona bond, causing expulsion of the weld metal at lower currents.

These statements are in good correspondence with the measurements of dynamic resistances (Section 3.3); however,

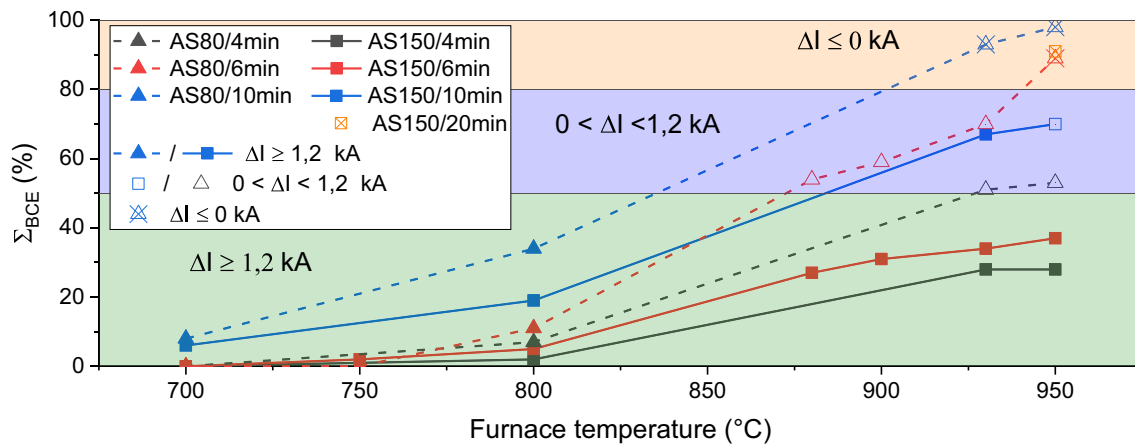


**Fig. 20** Correlation between  $\Sigma_{BCE}$  and WCR for 22MnB5 + AS80 and 22MnB5 + AS150

further investigations, involving studies of nugget development for different surface conditions and their correlation with the dynamic resistance, are required, to clarify the influence of surface layer on welding current range.

Considering that layer regions B, C, and E have a much higher resistance in comparison to the steel substrate and their influence on heat generation in the welding process, a criterion based on the fraction of these regions in the total layer thickness ( $\Sigma_{BCE}$ ), showing the relation between conductive and resistive phases in the layer, may be used to determine whether the material is joinable by analyzing the layer after the hot stamping process. As can be seen in Fig. 20, for the  $\Sigma_{BCE}$  under 50% determined weld current ranges for both coatings were higher than 1.2 kA, for layers with  $\Sigma_{BCE}$  between 50 and 80% a reduction of the WCR was observed, so that the determined WCR was lower than 1.2 kA and after  $\Sigma_{BCE}$  of 80% is exceeded no welding current range could be produced. This criterion, however, does not consider the above described adverse effects of high-conductive Al-Si (layer G) presence and can be used to assess joinability of heat-treated conditions at which the surface layer consists of intermetallic phases.

## 4 Conclusions

Influence of the heat treatment for a wider range of furnace temperatures and times, simulating manufacturing of tailored-property parts (tpp) by partial austenitization on the size and position of welding current ranges, was investigated for Zn- and Al-Si-coated 22MnB5. Following observations were made:

1. A correlation between contact resistance and welding current range depends on the coating:
  - 1.1. For 22MnB5 + Z140, a reduction of welding current range was observed for HT conditions, for which the

measured static contact resistance has exceeded the recommended maximal threshold of 1000  $\mu\Omega$

- 1.2. For 22MnB5 + AS, the static contact resistance increases with the decreasing fraction of metallic coating regions (at 700 °C), no correlation between the formation and growth of highly resistive intermetallic phases at high furnace temperatures (from 800 °C) and contact resistance was observed. The contact resistance threshold of 800  $\mu\Omega$  recommended in DVS 2935-3 for Al-Si-coated components could not be confirmed. For the material condition for which the threshold was exceeded (e.g., AS150/800 °C/6 min), a sufficiently large welding current range could be determined, for material conditions with the measured resistance values below the specified limit (AS80/930 °C/4 and 6 min) no welding current range could be determined.
2. For Al-Si coating, the size and position of the welding current range can be correlated with the layer development:
  - 2.1. At low furnace temperatures and short furnace times, when metallic Al-Si layer and phases with lower electrical resistance ( $Fe_2SiAl_7/Fe_2Al_5$ ) are present in the coating, a lower amount of heat is generated in the welding process, welding current range is shifted towards higher welding currents, but are still larger than 1.2 kA.
  - 2.2. With increasing furnace temperature and time intermetallic phases with high electric resistivity,  $Fe_2SiAl_2$ ,  $AlFe/Fe_3Al$ , and  $\alpha$ -Fe with Al (layers B, C, E) occur. Up to a total of 50% of these high-resistive phases in the layer  $\Sigma_{BCE}$ , welding current ranges larger than 1.2 kA were determined.
  - 2.3. Between  $\Sigma_{BCE}$  of 50 and 80%, the determined welding current ranges were lower than 1.2 kA.

- 2.4. Starting with the fraction  $\Sigma_{BCE}$  of more than 80%, no welding current range could be determined.
- 2.5. The proposed criterion  $\Sigma_{BCE}$ , considering fraction of resistive phases in the surface layer can be used to assess the joinability of Al-Si-coated parts based on metallographic analysis of surface layers.
- 2.6. For higher fraction of resistive phases, higher dynamic resistance was measured. However, to confirm this correlation, further investigations with the focus on dynamic resistance development, its influence on the heat input into the weld and changes in nugget growth kinetics, related with it on a wider palette of HT conditions are necessary.

**Acknowledgments** The authors would like to thank AiF for funding the IGF-Project IGF-Nr.:18.939B (DVS-Nr.: 04.060) of the Research Association on Welding and Allied Processes of the DVS, which was part of the program to support cooperative industrial research (Industrielle Gemeinschaftsförderung (IGF)) by the Federal Ministry for Economic Affairs and Energy, following a decision of the German Bundestag. Equal thanks go to all companies, colleagues, and students who contributed their support, knowledge, and effort to the project.

## References

1. Effenberg G, Landolt H, Börnstein R, Martienssen W, Madelung O (2005) Numerical data and functional relationships in science and technology. New series. Springer, Berlin
2. Drillet P, Spehner D, Kefferstein R Coated steel strips - European Patent Office - EP 2086755 B1. Abrufdatum 23.11.2018
3. Grigorieva R, Drillet P, Maigne JM, Redjaimia A (2011) Phase transformations in the Al-Si coating during the austenitization step. *Solid State Phenom* 172-174:784–790
4. Jenner F, Walter ME, Mohan Iyengar R, Hughes R (2010) Evolution of phases, microstructure, and surface roughness during heat treatment of aluminumized low carbon steel. *Metall Mater Trans A* 41(6):1554–1563
5. Windmann M, Röttger A, Theisen W (2014) Formation of intermetallic phases in Al-coated hot-stamped 22MnB5 sheets in terms of coating thickness and Si content. *Surf Coat Technol* 246:17–25
6. Janik V, Lan Y, Beentjes P, Norman D, Hensen G, Sridhar S (2016) Zn diffusion and  $\alpha$ -Fe(Zn) layer growth during annealing of Zn-coated B steel. *Metall Mater Trans A* 47(1):400–411
7. Ighodaro OL-R, Biro E, Zhou YN (2017) Study and applications of dynamic resistance profiles during resistance spot welding of coated hot-stamping steels. *Metall Mater Trans A* 48(2):745–758
8. Laurenz R, Ohse P (2012) Einfluss der Ofenverweilzeit von metallisch überzogenem Warmumformstahl auf die Eignung zum Widerstandspunkt-, Buckel- und Lichtbogenbolzenschweißen. *Schweißen und Schneiden* 64(10):654–661
9. Kuhlmann M, Mitzschke, Niels, Wohner, Maximilian, Jüttner S (2017) Einfluss von Prozessbedingungen beim Formhärten auf die Verbindungseigenschaften gefügter Bauteile. In: Merklein M, Warmblechumformung EW (eds) 12. Erlanger Workshop Warmblechumformung. Tagungsband zum 12. Erlanger Workshop Warmblechumformung: Erlangen, den 23. November 2017. Bamberg
10. Faderl J, Kolnberger S, Kurz T, Luckaender G, Manzenreiter T, Rosner M (2009) phs-ultraform@—continuous galvanizing meets press-hardening. In: Oldenburg M, Steinhoff K (eds) Hot sheet metal forming of high-performance steel. 2nd international conference; CHS2, June 15–17, 2009, Luleå, Sweden; proceedings; CHS2-series No. 2. Auerbach
11. Marc J van Genderen, Wico C Verloop, Jenny Loiseaux, Guido C Hensen (2011) Zinc-coated boron steel, ZnX@: direct hot forming for automotive applications. In: Oldenburg M, Steinhoff K (eds) Hot sheet metal forming of high-performance steel - CHS2. 3rd international conference; June 13–17, 2011, Kassel, Germany; proceedings; CHS2-series No. 3. Auerbach
12. Horn A, Merklein M (2018) Fertigung funktionsoptimierter Bauteile beim Presshärten. In: Merklein M, Hell H, Horn A (eds) 13. Erlanger Workshop Warmblechumformung. Tagungsband zum 13. Erlanger Workshop Warmblechumformung. Erlangen
13. Lehmann H, Etzold U (2018) Wärmebehandlungsanlage zum Thermischen Printen für das partielle Vergüten beim Presshärten. In: Merklein M, Hell H, Horn A (eds) 13. Erlanger Workshop Warmblechumformung. Tagungsband zum 13. Erlanger Workshop Warmblechumformung. Erlangen
14. Sherepenko O, Schreiber V, Schischin I, Luo Y, Wernlein P, Jüttner S (2019) Einfluss des Oberflächen- und Werkstoffzustandes auf die Punktschweißneigung partiell gehärteter Bauteile mit Al-Si Beschichtungen. In: DVS Media GmbH (ed) 24. DVS-Sondertagung Widerstandsschweißen. Treffpunkt Widerstandsschweißen
15. Deutscher Verband für Schweißen und verwandte Verfahren e.V.: DVS 2929–1. Messung des Übergangswiderstands, Grundlagen, Messmethoden und -einrichtungen (2014)
16. Deutscher Verband für Schweißen und verwandte Verfahren e.V.: DVS 2935–3. Widerstandspunktschweißen von Feinblechen aus niedrig legierten Stählen, Presshärtende Stähle (2019)
17. Deutsches Institut für Normung e.V.: Prüf- und Dokumentationsrichtlinie für die Fügeignung von Feinblechen aus Stahl - Teil 2: Widerstandspunktschweißen (2011) 1220-2. Berlin
18. Fan DW, de Cooman BC (2012) State-of-the-knowledge on coating systems for hot stamped parts. *Steel Res Int* 83(5):412–433
19. Horie T, Niho T, Hayashi N, Ishihara D (2019) Cycles of triply coupled mechanical contact, current, and thermal conduction phenomena during resistance spot welding. *Weld World* 63:126
20. Windmann M, Röttger A, Theisen W (2013) Phase formation at the interface between a boron alloyed steel substrate and an Al-rich coating. *Surf Coat Technol* 226:130–139
21. Lilly AC, Deevi SC, Gibbs ZP (1998) Electrical properties of iron aluminides. *Mater Sci Eng A* 258(1–2):42–49
22. Pazourek A, Pfeiler W, Šima V (2010) Dependence of electrical resistivity of Fe–Al alloys on composition. *Intermetallics* 18(7):1303–1305
23. Wink H-J, Krätschmer M (2012) Charakterisierung und Modellierung des Bruchverhaltens von Punktschweißverbindungen in pressgehärteten Stählen. Teil II - Simulation des Schweißens. Ulm
24. Brandes EA, Brook GB, Smithells CJ (1998) In: Brandes EA, Brook GB (eds) Smithells metals reference book, 7th edn. Butterworth-Heinemann, Oxford, Boston
25. Meyer R (2012) Erhöhung der Prozesssicherheit durch Beherrschung der Bauteilabweichung beim Fügen im Karosseriebau. TUDpress, Dresden
26. Saha DC, Ji CW, Park YD (2015) Coating behaviour and nugget formation during resistance welding of hot forming steels. *Sci Technol Weld Join* 20(8):708–720

**Publisher's note** Springer Nature remains neutral with regard to jurisdictional claims in published maps and institutional affiliations.